AGU PUBLICATIONS

JGR

Journal of Geophysical Research: Oceans

RESEARCH ARTICLE

10.1002/2015JC010772

Key Points:
- Melting icebergs are continuous source of meteoric meltwater
- Volume of the *Near-field* has been computed
- Scale to the larger population of icebergs

Correspondence to:
J. J. Helly,
hellyj@ucsd.edu

Citation:
Helly, J. J., M. Vernet, A. E. Murray, and G. R. Stephenson Jr. (2015), Characteristics of the meltwater field from a large Antarctic iceberg using $\delta^{18}O$, *J. Geophys. Res. Oceans*, *120*, 2259–2269, doi:10.1002/2015JC010772.

Received 10 FEB 2015
Accepted 20 FEB 2015
Accepted article online 25 FEB 2015
Published online 27 MAR 2015

Characteristics of the meltwater field from a large Antarctic iceberg using $\delta^{18}O$

John J. Helly[1,2], Maria Vernet[2], Alison E. Murray[3], and Gordon R. Stephenson Jr.[4]

[1]San Diego Supercomputer Center, University of California, San Diego, La Jolla, California, USA, [2]Scripps Institution of Oceanography, University of California, San Diego, La Jolla, California, USA, [3]Desert Research Institute, Reno, Nevada, USA, [4]School of Ocean Sciences, Bangor University, Anglesey, UK

Abstract Large tabular icebergs represent a disruptive influence on a stable water column when drifting in the open ocean. This is a study of one iceberg, *C18A*, encountered in the Powell Basin in the Weddell Sea in March 2009, formed from iceberg *C18* (76×7 km) originating from the Ross Ice Shelf in May 2002. *C18A* was lunate in shape with longest dimensions of 31 km×7 km×184 m. The meltwater field from *C18A* was characterized using $\delta^{18}O$ from water samples collected near *C18A* (*Near-field*, 0.4–2 km) and contrasted with a *Far-field* comprised of samples from an *Away* site (19 km from *C18A*), a *Control* site (70 km away), and a region populated with small icebergs (*Iceberg Alley*, 175 km away). The in-sample fractions of meteoric water were calculated relative $\delta^{18}O$ in iceberg ice and Weddell Deep Water and converted to meteoric water height (m) and a percentage within 100 m depth bins. The *Near-field* and *Far-field* difference from surface to 200 m was 0.51±0.28%. The concentration of meteoric water dropped to approximately half that value below 200 m, approximate keel depth of the iceberg, although detectable to 600 m. From surface to 600 m, the overall difference was statistically significant ($P < 0.0001$). From this, we estimate the *Near-field* volume astern of the iceberg (0.16 $km^3 d^{-1}$) as a continuous source of meteoric water.

1. Introduction

A massive inventory of icebergs, ranging in size from growlers and bergy bits to very large tabular icebergs, circulates around the Antarctic continent. On average, there are an estimated 2×10^5 icebergs in the Southern Ocean with linear dimensions greater than 50 meters (m) [*Orheim*, 1988; *Williams et al*., 1999]. The majority of these range from 60 to 2200 m in length, with thicknesses that vary from 150 to 550 m [*Gladstone et al*., 2001].

Large tabular icebergs originate from ice shelves in the Ross, Bellingshausen, and Weddell Seas [*Scambos et al*., 2008; *Long et al*., 2002; *Lazzara et al*., 1999] and become entrained in the counterclockwise, circumpolar countercurrent (Antarctic Coastal Current). This standing mass of icebergs is comparable in magnitude ($\sim10^{15}-10^{16}$ kg) [*Silva et al*., 2006; *Tournadre et al*., 2012] to the maximum mass of seasonal sea ice that surrounds Antarctica [*Timco and Frederking*, 1996; *Cavalieri and Parkinson*, 2008; *Worby et al*., 2008]. *Silva et al*. [2006] estimated that giant icebergs accounted for half the mass loss of the Antarctic ice sheet over the 25 year period from 1979 to 2003; approximately 1.1 $\times10^{15}$ kg yr^{-1}. More recently, *Rignot et al*. [2013] estimated mass loss from calving to be 1089±139 $Gtyr^{-1}$ ($1.1\pm0.14\times10^{15}$ $kgyr^{-1}$) and from basal ice-shelf melting at 1325±235$Gtyr^{-1}$ ($1.3\pm0.24\times10^{15}$ $kgyr^{-1}$).

Icebergs shrink with age due to ablation: a combination of melting, fracturing, calving, wave-enhanced erosion, sublimation, and evaporation [*Kristensen*, 1983; *Scambos et al*., 2005]. To the east of the Antarctic Peninsula and west of the South Orkney Islands, a strong northward flow in the northwestern Weddell Sea [*Thompson et al*., 2009] concentrates large numbers of ablating icebergs of all sizes from various locations around Antarctica [*Ballantyne*, 2002; *Schodlok et al*., 2006] after being transported into the southeastern Weddell Sea by the counterclockwise Antarctic Coastal Current [*Stuart and Long*, 2011]. Within the Weddell Sea, the Larsen and Filchner-Ronne ice shelves are local sources of iceberg production as well.

Meltwater from the ablating icebergs alters the geophysical, chemical, and biological properties of the ambient seawater in which it is deposited and mixed [*Smith*, 2011a]. Likewise, seawater surface-mapping

Table 1. Range of $\delta^{18}O‰$ Values in Major Antarctic Water Reservoirs

Reservoir	Spatial Domain	$\delta^{18}O‰$ Range or $\bar{x} \pm$SD	Reference
Antarctic ice sheet surface	Continental	[−57, −9.5]	*Morgan* [1982]
Glacial ice core	Filchner-Ronne Ice Shelf	[−33.5, −26]	*Oerter et al.* [1992]
Precipitation	Western Antarctic Peninsula	∼−20	*Meredith et al.* [2008]
Glacial meltwater	Western Antarctic Peninsula	∼−13	*Meredith et al.* [2008]
Antarctic surface water (AASW)	Weddell Sea	[−0.35, −0.30]	*Weiss* [1979]
Winter water (WW)	Weddell Sea	[−0.30, −0.23]	*Weiss* [1979]
Warm deep water (WDW)	Weddell Sea	[−0.05, −0.01]	*Weiss* [1979]
Circumpolar deep water (CDW)	Continental	−0.07±0.024	*Jacobs and Fairbanks* [1984]

[*Helly et al.*, 2011a, 2011b] and hydrocasts through the pycnocline [*Stephenson et al.*, 2011] have been used to describe the *Near-field* and *Far-field* spatial and temporal distributions of salinity and temperature in relation to a large free-drifting iceberg.

Turbulent structures and vertical advection have also been reported in association with icebergs in the North Atlantic and Antarctica [*Pisarevskaya and Popov*, 1991; *Pisarevskaya and Volkov*, 2007]. Those results are consistent with the convection of warm water near icebergs [*Neshyba*, 1977] in the Antarctic and penetration of the Atlantic water heat to the upper layer of the Arctic Ocean through transient apertures in the pycnocline.

1.1. Oxygen Isotopes

Here we report new results using $\delta^{18}O$ to derive an estimate of the meteoric water fraction contributed by an iceberg to ambient seawater. The hydrological context for using $\delta^{18}O$ as a tracer to determine the source of water is based on the fractionation of the oxygen isotopes in water molecules, by both evaporation and condensation, into molecules containing the lighter (O^{16}) or heavier (O^{18}) isotopes of oxygen. Lighter water molecules containing O^{16} evaporate more readily, so precipitation resulting from the evaporated light water is enriched in O^{16} and depleted in O^{18} relative to a seawater standard. At the surface of the ocean, $\delta^{18}O$ is increased by evaporation and decreased by precipitation while away from the surface it is a conservative tracer [*Meredith et al.*, 2008].

Oxygen isotopic results are reported in parts per thousand (‰) relative to VSMOW (Vienna Standard Mean Ocean Water) and normalized such that the oxygen isotopic values of Standard Light Antarctic Precipitation (SLAP) are −55.5‰ according to equation (1) [*Coplen*, 1994].

$$\delta^{18}O‰ = \left(\frac{\left(\frac{^{18}O}{^{16}O}\right)_{sample}}{\left(\frac{^{18}O}{^{16}O}\right)_{standard}} - 1 \right) \times 1000 \quad (1)$$

The glacial ice that covers Antarctica is supplied by precipitation (meteoric water) and therefore has a value of $\delta^{18}O < 0$, signifying that it is depleted in $\delta^{18}O$ relative to the VMSOW. By contrast, values of $\delta^{18}O > 0$ are characteristic of deeper ocean waters not in contact with the atmosphere. Values for Antarctic ecosystems dominated by atmospheric deposition (e.g., glaciers) range from −57‰ to −13‰, while seawater values range from −0.35‰ to −0.05‰ (Table 1).

Large tabular icebergs are masses of glacial ice that have been set adrift; they therefore have meteoric values of $\delta^{18}O < 0$. Icebergs are distinct from sea ice in this regard. Sea ice shares the ambient isotopic signature of the seawater out of which it has frozen [*Lehmann and Siegenthaler*, 1991]. Factors that affect $\delta^{18}O$ in Antarctic seawater include meteoric water (i.e., glacial meltwater and local precipitation) and advection of sea ice that may nonconservatively import or export water molecules.

By analyzing water samples collected near and far from an iceberg and applying a mixing model, we estimate (1) the marginal concentration of meteoric water in the ocean due to the presence of a large iceberg, (2) the daily ablation rate of a large tabular iceberg, and (3) the quasi-static amount of freshwater attributable to the iceberg's presence (i.e., a persistent, *Near-field* and *Far-field* that slowly mixes back to ambient conditions).

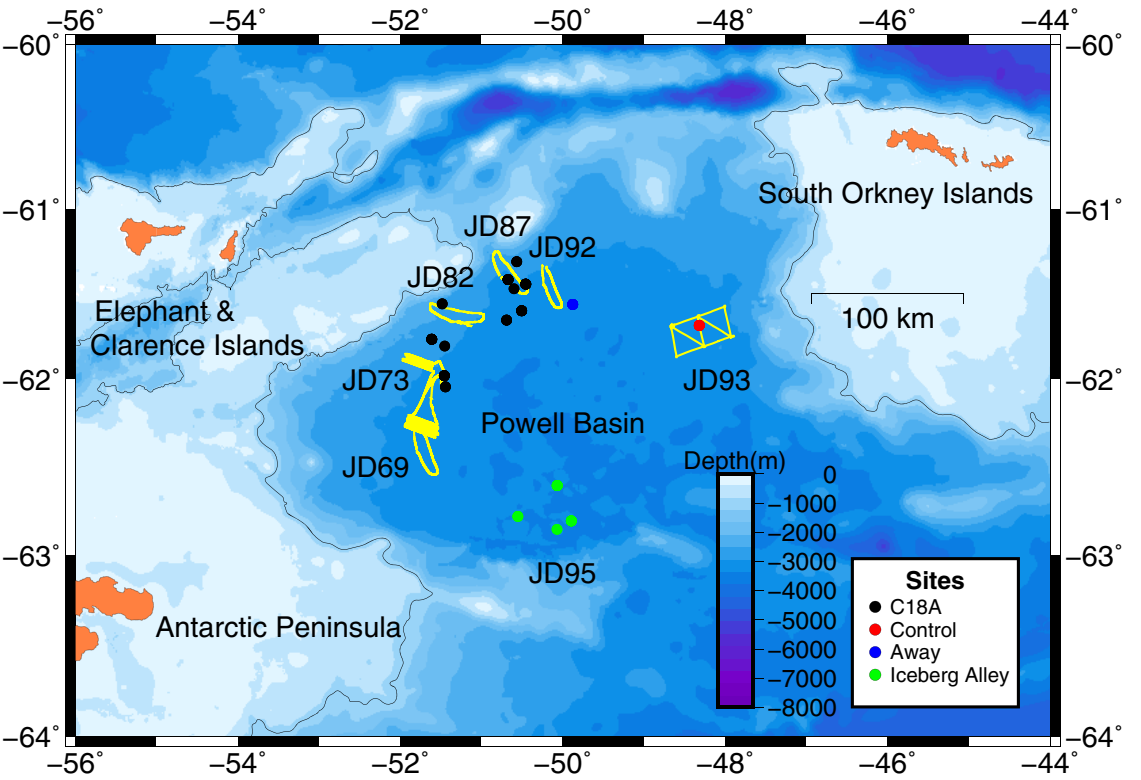

Figure 1. Location of iceberg *C18A* (yellow) from 10 March 2009 to 3 April 2009 determined by circumnavigating the iceberg on a given Julian day (JD) and extracting that time period from the GPS navigation data (ship track). The location of the *Control* site is also shown by the same method. The −1000 m contour is shown for depth reference.

1.2. Water Masses

The Weddell Sea (Figure 1) has distinct water masses that are characterized by their temperature and salinity [*Weiss*, 1979; *Jacobs and Fairbanks*, 1984; *Garabato et al*., 2002; *Stephenson et al*., 2011]. Those of interest in this study are, in order from the surface to depth: Antarctic surface water (AASW), winter water (WW), Warm Deep Water (WDW), which is a type of circumpolar deep water (CDW) [*Garabato et al*., 2002], and Weddell Sea Deep Water (WSDW). Below WSDW is Weddell Sea Bottom Water (WSBW) which, when exported out of the Weddell Sea, contributes to Antarctic Bottom Water (AABW).

AASW is formed from WDW that is modified by interactions with the atmosphere, meteoric water, and a seasonal air temperature minimum [*Jacobs and Fairbanks*, 1984]. Consequently, it is a mixing product of meteoric water (precipitation and glacial ice, including icebergs) and WDW. These two sources, meteoric water from a calved piece of *C18A* ice and WDW, are used as end-members in the estimation of meteoric water fraction in section 2.1.

Sea ice concentrates brine in the surface water when it freezes and freshens it when it melts. This tends to enrich the sea ice in ^{18}O while depleting the seawater. If sea ice is advected into or out of a sample area, it can violate the conservation of $\delta^{18}O$ in a manner similar to the evaporation and precipitation processes at the surface (cf. section 1.1). Below the surface $\delta^{18}O$ is a conservative tracer.

2. Methods

Sixty-five hydrocasts were performed in the Powell Basin of the northwest Weddell Sea on-board the RVIB Nathaniel B. Palmer (Cruise NBP0902) east of the Antarctic Peninsula during March and April 2009 in order to study the effects of iceberg *C18A* on the ecosystem. *C18A* formed from iceberg *C18* (76×7 km) originating from the Ross Ice Shelf in May, 2002. *C18A* was lunate in shape with longest dimensions of 31 km×7 km×184 m. Figure 1 depicts our study site in this region bounded by (W52°, S61°) and (W47°, S63°) with the ship track showing circumnavigations of *C18A*, surface mapping of the wake field and surface

Table 2. Characteristic Values of End-Member Water Sources Related to Figure 2 in March to April 2009

End-Member and Source	Salinity (PSS)	Temperature (°C)	$\delta^{18}O$(‰)
WDW [*Stephenson et al.*, 2011; *Weiss*, 1979]	34.75	0.5	−0.05
Iceberg ice (Measured; possibly contaminated by seawater infiltration)	5.0	−10.0	−17.92

mapping of the *Control* site as well as the location of the sample sites: *C18A*, *Away*, *Control*, and *Iceberg Alley* (*IA*). The sampling methodology is described in *Helly et al*. [2011a] and *Stephenson et al*. [2011].

Hydrocasts taken between 0.4 and 2 km from *C18A* are classified as the *C18A* site and also referred to as the *Near-field*. The *Far-field* includes the *Away* site, 19 km from *C18A* at the time it was sampled, the *Control* site was 70 km east of *C18A*, and the *Iceberg Alley* site which was 175 km southeast of *C18A* and contained many small icebergs and bergy bits. The *Control* site was without iceberg traffic for at least 2 weeks prior to sampling based on direct observations by microwave satellite imagery resolving icebergs >4 km in longest dimension. A set of 107 discrete water samples was collected by hydrocast across the sites. A few of these samples were collected from the surface using a towfish [*Lin et al*., 2011] but most were collected by Niskin bottles at discrete depths. Of 65 CTD casts performed during the cruise, 56 were deeper than 250 m, with most of these profiles going deeper than 500 to ~600 m [*Stephenson et al*., 2011]. Samples (80 mL) were sealed and transported back to the Scripps Institution of Oceanography, stored at ambient temperature, and subsequently sent to the USGS Reston Stable Isotope Laboratory for isotopic analysis. Water samples were analyzed for $\delta^{18}O$ (equation (1) [*Coplen*, 1994]) using the CO_2 equilibration technique of *Epstein and Mayeda* [1953] and automated by *Révész and Coplen* [2008]. The error in these measurements is ±0.03%.

A dense, blue *C18A* ice fragment was collected from an observed sidewall calving event. Thus it was well below the unconsolidated surface (firn) of recently accumulated meteoric water and not from the bottom of the iceberg. This fragment was also measured for $\delta^{18}O$ using the method described above but the salinity was measured by a hand-held refractometer with a precision of 0.014 on the practical salinity scale (PSS). The salinity of the fragment was 5 PSS (Table 2). The salinity of meteoric water is theoretically zero and this is the value used by *Meredith et al*. [2008] in a similar type of study. The ice-fragment may have been infiltrated by seawater after the calving event we observed before it was recovered from the sea.

2.1. Estimation of Meteoric Water Fraction

To analyze the component sources of each of the water samples, we applied the method of *Jenkins* [1999] and *Jenkins and Jacobs* [2008]. (The nomenclature used here is that of *Jenkins* [1999]. The superscripts are to be read as labels rather than as exponents.) For seawater that is a heterogeneous mixture of two known end-members, a composite property, ψ, can be defined using any two jointly conserved properties of the seawater (χ^1, χ^2) so that composite property $\psi^{2,1}$ is identically zero; zero everywhere along the line defined by equation (2).

$$\psi^{2,1} = (\chi^2 - \chi_0^2) - (\chi^1 - \chi_0^1)\left(\frac{\chi^2 - \chi_0^2}{\chi^1 - \chi_0^1}\right) \tag{2}$$

Nonzero values of $\psi^{2,1}$ represent nonconservative mixing processes or an input from outside the system, such as meltwater from sea ice or an iceberg. This study uses salinity and $\delta^{18}O$ as conservative tracers used to define the composite property $\psi^{2,1}$. This model provides a convenient two-dimensional way to visualize the parameter space of mixing and establishes a range of values to use for the end-members used in the calculation of meteoric water fraction. In this study, we are using $\delta^{18}O$ as the one-dimensional domain to estimate the meteoric water fraction.

We define ambient seawater along the line-of-conservation as a mixture of Warm Deep Water (WDW) and glacial ice using characteristic values of salinity and $\delta^{18}O$ for these end-members (Table 2). Given equation (1), by defining WDW as one end-member and glacial ice as the other we can then use equation (3) to estimate the fraction (Q_i) of meteoric water in each sample.

$$Q_i = \frac{(\delta^{18}O_i - \delta^{18}O_{WDW})}{(\delta^{18}O_{ice} - \delta^{18}O_{WDW})} \tag{3}$$

Uncertainty in Q_i is a function of uncertainty in the $\delta^{18}O$ measurement (±0.0001‰), the magnitude of the measured sample (numerator) plus the uncertainty in the measurement of the reference ice (denominator)

and its magnitude (Table 2). So, assuming independence of measurements such that the covariance is zero between the numerator and the denominator, the uncertainty in Q_i varies over [0.0002, 0.0025] for the Q_i values ranging over [0.0022, 0.0262] in a data-dependent way over the range of values of $\delta^{18}O$ [−0.4700, −0.0400].

Error propagation in the meteoric water fraction calculation followed standard methods [*NIST*, 2012]. The RMSE (square-root of the sum of mean squared deviations) values were computed using standard deviations obtained by the SAS/STAT software, Version 9.3 of the SAS system [*copyright*] for Linux. Plotting and curve-fitting were done with R [*R Development Core Team*, 2008] using the ggplot2 library. The LOESS smoothing option was chosen to provide a locally fitted polynomial with a 95% confidence interval using methods first described by *Cleveland* [1979]. The difference in meteoric water fraction between *Near-field* and *Far-field* sites was tested using a two-way analysis of variance (ANOVA).

Note that salinity is not used in the calculation of the meteoric water fraction. Therefore, the fact that the salinity of the iceberg-fragment end-member is nonzero has no effect on any of the subsequent analysis although it would slightly lessen the slope of the line-of-conservation (equation (2)) as discussed in section 3. The slope does not enter into any calculation. Furthermore, we assume a negligible amount of local precipitation such that ambient conditions were identical across sites including sea ice transport; no net import or export during the time of the study. A model of the *Near-field* meltwater volume, based on the meteoric water fraction, will be developed in section 3.

3. Results

Salinity values for all sites have fully overlapping ranges [33.65–34.50] from the surface to about 50 m indicating similar amounts of freshening in the mixed layer (Figure 2a). However, the corresponding $\delta^{18}O$ measurements only partially overlap [−0.42 to −0.3] and reveal distinctly different sources for the freshening (Figure 2b). At *C18A*, from the surface to 600 m, the $\delta^{18}O$ values are clearly more negative and distinct from the non-*C18A* sites.

Figures 2c and 2d show the same data reclassified into the *C18A* (*Near-field*) and *Far-field* sites to better illustrate the trends (Figures 2c and 2d). The sites have been fitted with LOESS regression lines depicting the 95% confidence interval around the fits. Figures 2c and 2d show mixed layer features in salinity and Q_i that mix back to deep water, ambient values of salinity [34.5–34.75] and $\delta^{18}O$ [−0.2 to −0.05] with inflection points in the fitted lines above 100 m but with significant differences that persist to about 500 m; considerably below the keel-depth of *C18A*.

We estimated the (1) meteoric water fraction (Q_i) for *Near-field* and *Far-field* sites, (2) difference between the sites by 100 m depth bin, (3) difference in the height of meteoric water equivalent, and (4) difference in the concentration of meteoric water as a percentage. The largest percentage difference in meteoric water concentration (Table 3) is in the surface to 100 m bin [0.52%] although this difference is relatively constant in the 100−200 m [0.49%] and 200−300 m [0.43%] bins after which the difference is reduced by ∼50% yet persists to 600 m [0.25−0.28%].

The fractions of meteoric water were significantly different between the *Near-field* and *Far-field* sites (ANOVA, $P < 0.0001$). Further, and not as surprising, significant differences (ANOVA, $P < 0.0001$) were observed between the surface depth bin values and all deeper water depth bins to 600 m at both site locations. From this, we conclude there is a similar depth-gradient of meteoric water at *Near* and *Far-field* locations, but the iceberg increased the meteoric water fraction by 0.37% over the integrated depth to 600 m in the *Near-field*.

In summary, the results show the meltwater from *C18A* to be a source of meteoric water input into an ambient ocean (Figures 2e and 2f) above and below the WW and the permanent pycnocline. Consequently, there is a quasi-static *Near-field* source of meteoric water attached to a moving iceberg. While the iceberg ablates, this provides input into a depth-stratified, ambient background (AASW, WW, WDW) that gradually mixes back, through a *Far-field* trace, to the ambient condition.

3.1. Geometric Model and *Near-Field* Volume Estimate

Meltwater fraction estimates were combined with a daily ablation rate estimate for *C18A* to construct a geometric model of the *Near-field* source attached to *C18A* as it ablates over its lifetime. *C18A* was imaged by

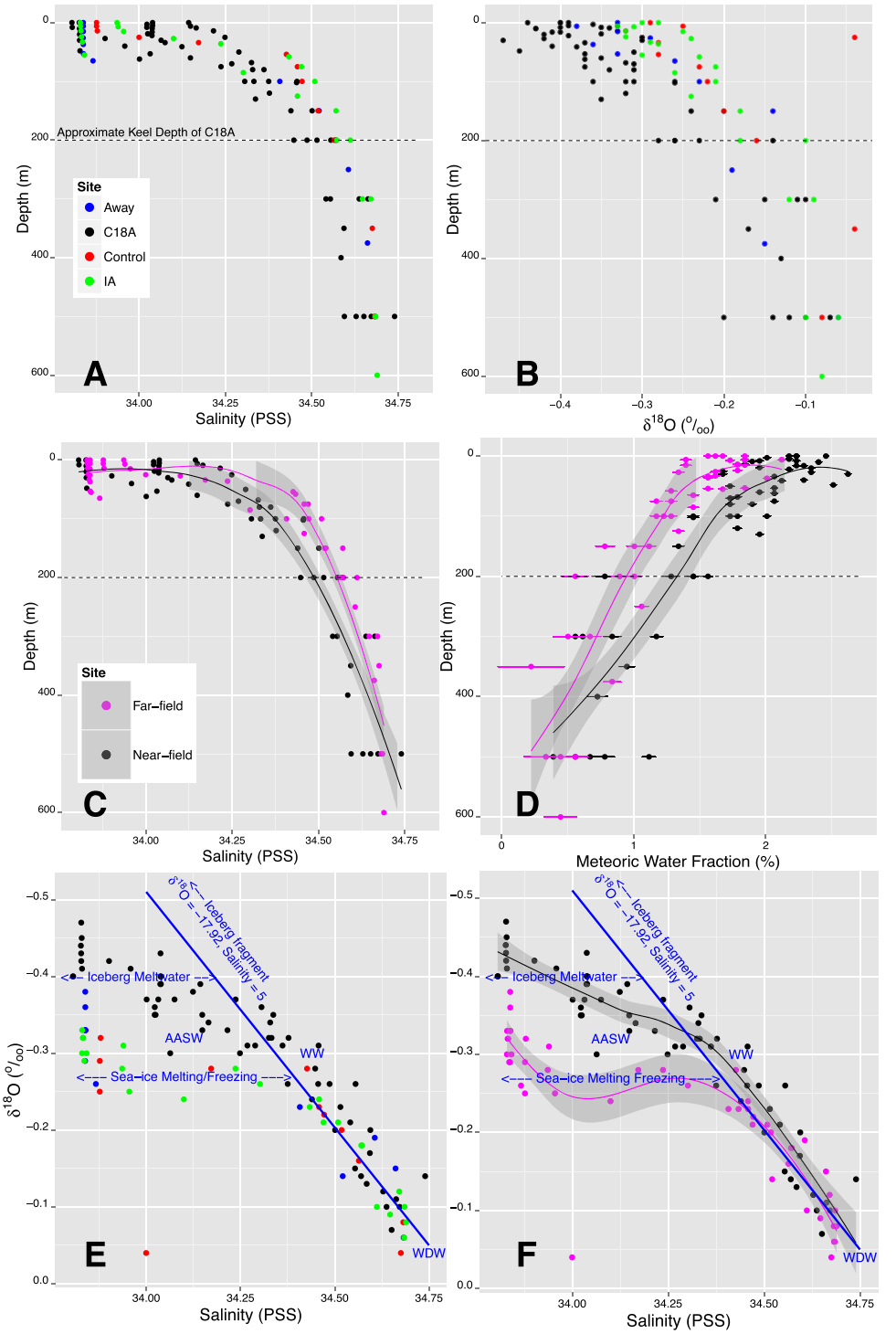

Figure 2. (a and b) $\delta^{18}O$ and salinity by depth and sampling site, respectively. (c) The LOESS fits (gray shading indicated 95% confidence interval) for salinity versus depth where the data have been grouped into *C18A* and *Far-field* sites. (d) The meteoric water fraction calculated according to *Jenkins and Jacobs* [2008] and *McDougall* [1990] (±SD) grouped the same as Figure 2c. (e and f) The [$\delta^{18}O$, salinity] parameter space. The dashed blue line is the line-of-conservation of mixing between glacial ice and WDW. Figure 2e depict the data by site and Figure 2f depict it according to the same grouping as Figures 2c and 2d.

the Quikscat scatterometer sensor for 257 days after the initial date we visited it to the time it disappeared from view (<4km in longest dimension) based on the database described by *Long et al*. [2002]. This interval was then used to estimate a fractional ablation rate of $\frac{1}{257}$ per day or 3.9×10^{-3}day^{-1} (Table 4). From this,

Table 3. Estimated Meteoric Water Fractions (Q_i) by 100 m Depth Bin and Sampling Site[a]

Depth (z) Bin (m)	*Near-Field* ($\bar{x} \pm$SD)	*Far-Field* ($\bar{x} \pm$SD)	Difference ($\Delta\bar{x} \pm$RMSE)	Meteoric Water Equivalent (Δm)	Meteoric Water Concentration (Δ%)
$0 \leq z < 100$	0.0209 ± 0.0025 (N = 35)	0.0157 ± 0.0035 (N = 28)	0.0052 ± 0.0043	0.52 ± 0.43	0.52 ± 0.43
$100 \leq z < 200$	0.0163 ± 0.0030 (N = 9)	0.0113 ± 0.0019 (N = 7)	0.0049 ± 0.0036	0.49 ± 0.36	0.49 ± 0.36
	Summed to Iceberg Keel Depth			1.01 ± 0.56	0.51 ± 0.28
$200 \leq z < 300$	0.0131 ± 0.0031 (N = 5)	0.0088 ± 0.0022 (N = 4)	0.0043 ± 0.0038	0.43 ± 0.38	0.43 ± 0.38
$300 \leq z \leq 400$	0.0081 ± 0.0023 (N = 6)	0.0056 ± 0.0026 (N = 4)	0.0025 ± 0.0035	0.25 ± 0.35	0.25 ± 0.35
$400 < z < 500$	0.0075 ± 0.0035	0.0049 ± 0.0029	0.0027 ± 0.0045	0.27 ± 0.45	0.27 ± 0.45
$500 \leq z \leq 600$	0.0070 ± 0.0027 (N = 5)	0.0042 ± 0.0012 (N = 5)	0.0028 ± 0.0030	0.28 ± 0.30	0.28 ± 0.30
	Summed to WDW Depth			2.24 ± 0.94	0.37 ± 0.13

[a]Two samples were treated exceptionally. A *C18A* sample at 400 m was included with the 300 m depth bin and a *Far-field* sample at 600 m was included in the 500 m depth bin. This was done because these were the only samples in those depths at either site. Note that this is reflected in the different depth bin limits at those depths. The values for depth bin 400−500 were interpolated from adjacent vertical layers.

we calculated a mean daily mass loss from *C18A* and the volume for the meltwater *Near-field* using the total meteoric water fraction from Table 3. These values were used to define a preliminary model of the geometry the field. The meltwater field, with stationary volume (V_q), is assumed to be solely a function of iceberg size, neglecting weather, tides, and currents, extending astern away from the mean direction of iceberg motion.

V_q was modeled as a set of n vertically stacked ellipses with shape parameters (α, β) varying by depth bins of arbitrary thickness (ζ_i) each with a corresponding meteoric water fraction (δ_i) (Table 3). The shape parameters define the length of the major and minor axes of each ellipse.

Consequently, we estimated the quasi-static *Near-field* volume to be:

$$V_q = \left(\sum_{i=1}^{n} \zeta_i \delta_i \alpha_i \beta_i \pi \right) - V^d_{iceberg} \tag{4}$$

where V_d is the displacement volume of the iceberg contained within the elliptical volume. This expression was simplified by integrating across the water column and centering the ellipse on the end of the iceberg. This results in:

$$V_q = \frac{\Delta_Q}{2} (z \pi \alpha \beta) \tag{5}$$

Here Δ_Q is the meteoric water fraction (Q) integrated over the 0–200 m depth range from Table 3, 0.0051±0.0028. We know that the speed of *C18A* was 8.8 km d^{-1} [*Helly et al*., 2011a] so we use this distance to estimate β. The water depth (z) is set at 200 m since this is approximately the keel-depth of *C18A* and just above the transition to the lower concentration bin (Table 3).

Then, V_q is computed from the daily mass ablated from *C18A*, converted to a volume ($V_q = M_A \rho^{-1}_{meltwater}$). This leaves the only unknown, α, to be estimated at 11.5 km. These calculations are summarized in Table 4. The result is a half-ellipsoidal volume (V_q) centered on the end of *C18A* that is 23 km wide (i.e., 11.5 km on each side) and extending 8.8 km behind *C18A* from the surface to a depth of 200 m with a 0.51% mean concentration of meltwater due to the presence of *C18A*.

4. Discussion

The use of $\delta^{18}O$ as a tracer of iceberg-derived meteoric meltwater built upon previous efforts to delineate the spatial and temporal extent of the *C18A* meltwater field and to assess it as a source of disturbance to the ambient marine environment [*Helly et al*., 2011a, 2011b]. Previously, the temporal and spatial scales, both horizontal and vertical, of *C18A*'s effects were defined based on temperature and salinity parameters. Those characteristics provided a framework to quantify the meteoric water injection by *C18A* ablation in this study allowing us to develop an improved model of how the meteoric meltwater affected water

Table 4. Iceberg Physical Dimensions and Ancillary Parameters[a]

Parameter	Source	Estimate
Length (L)	*Helly et al.* [2011a]	3.11×10^4 m (31.1 km)
Width (W)	*Helly et al.* [2011a]	7.0×10^3 m (7.0 km)
Freeboard elevation (h_s)	*Helly et al.* [2011a]	2.8×10^1 (28 m)
Keel depth (Z)	*Helly et al.* [2011a]	1.84×10^2 m (184 m)
Total height (H)	$H=h_s+Z$	2.12×10^2 m (212 m)
Total volume (V_t)	$V_t=HLW$	$4.6\times10^{10}\mathrm{m}^3(46\,\mathrm{km}^3)$
Total mass (M_{C18A})	$\rho_{sw}(LWZ)$	4.11×10^{13} kg (41.1 Gt)
Firn depth (F)	$\mathrm{H}\frac{(M_{C18A})\rho_{ice}^{-1}}{LW}$	5 m
Ice density (ρ_{ice})	*Wadhams* [2000]	$917\,\mathrm{kgm}^{-3}$
Seawater density (ρ_{sw}) $[-1,5]^\circ$C	*Wadhams* [2000]	$1030\,\mathrm{kgm}^{-3}$
Meltwater field density (ρ_{field})	Interpolated from *Wadhams* [2000]	$1015\,\mathrm{kgm}^{-3}$
Meltwater density ($\rho_{meltwater}$)	Interpolated from *Wadhams* [2000]	$1005\,\mathrm{kgm}^{-3}$
Daily ablation rate from scatterometer (k_A)	$k_A=100\times\frac{1}{257}$ days calculated from tracking data [*Long et al.*, 2002]	0.4 % d^{-1}
Daily ablation mass (M_A)	$M_A=k_AM_{C18A}$	1.6×10^{11} kg d^{-1} (0.16 Gt d^{-1})
Daily quasi-static meltwater volume (V_q)	Equation (5)	$1.6\times10^8\mathrm{m}^3\mathrm{d}^{-1}$ (0.16 km^3 d^{-1})

[a]Standard units are provided for ease-of-calculation. Scaled values are provided in parentheses for convenient intercomparison with other studies (Gigaton(Gt)$=10^{12}$ kg).

column structure. This provided a means to derive a volumetric estimate of the distribution and differential concentration of the meteoric water from *C18A* relative to the ambient environment.

4.1. Comparison With Prior Meltwater Concentration Estimates

These results are similar to results from our earlier studies, using different methods, and support these estimates as realistic values for meteoric water concentrations in the *Near-field* of an iceberg such as *C18A*. *Stephenson et al.* [2011] developed estimates of *C18A* basal meltwater production also using a mixing model approach but based on temperature and salinity using a different method. The result from that approach, 0.2 m of water column height within 100–200 m depth bin, is within the confidence interval of our estimate (0.49 ± 0.36 m, Table 3). Some assumptions of that study may be violated in our analysis due to ablation of the subaerial portions of *C18A* through wave action and sun-induced melting. Similar end-member limits were defined for WDW, AASW, and WW using temperature and salinity but the meteoric water fraction was estimated by constraining the fine-structure mixing revealed in CTD profiles along an isopycnal so that the point of intersection with a limit lines could be determined.

4.2. Choice of $\delta^{18}O$ Glacial End-Member

The choice of the $\delta^{18}O$ end-members for the meteoric water fraction (Q_i) estimates is an important determinant of our results since they determine the value of the denominator in equation (3). The dense, blue *C18A* ice fragment we chose came from an observed sidewall calving event. Thus it was well below the unconsolidated surface (firn) of recently accumulated meteoric water and not from the bottom of the iceberg. The other end-member, for WDW, comes from the literature as indicated in Table 2 and is well established.

The iceberg ice $\delta^{18}O$ values ($-18‰$) are slightly enriched relative to some ice-shelf values and similar to values for glacial meltwater. *Grootes and Stuiver* [1983] found values on the Ross Ice Shelf to range from about $-34‰$ to $-27‰$ from approximately 40 to 200 m in the ice-shelf. These results are similar to those reported by *Oerter et al.* [1992] ($-33.5‰$ to $-26‰$) for the Filchner-Ronne ice shelf raising the question as to whether our value is representative of the overall meteoric water composition of *C18A*. Interestingly, the keel-depth of *C18A* (184 m) is within what *Oerter et al.* [1992] identified as a *marine shelf ice* that is formed from seawater with a $\delta^{18}O > 0$. Such a shelf could be exposed to higher $\delta^{18}O$ values from seawater that may melt, mix, and refreeze onto the glacier resulting in intermediate values within the glacial ice. Our values are consistent with the values measured in Marguerite Bay, Antarctic Peninsula by *Meredith et al.* [2008] for precipitation ($-13‰$) and glacial meltwater ($-20‰$).

Although we do not have a control for this uncertainty, based on what is known about iceberg formation, we argue that the measured $\delta^{18}O$ of the *C18A* fragment is a reasonable value to use in this analysis.

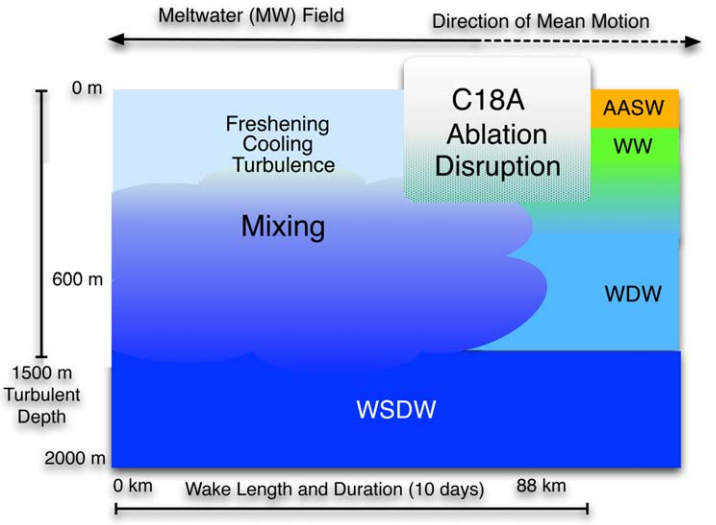

Figure 3. Oblique view of a three-dimensional model of *C18A* with its quasi-static meltwater *Near-field* and dispersive *Far-field* approximately to scale. The *Near-field* is a half-ellipsoid (23.5 × 8.8 km) with a depth reaching to approximately 200 m and meltwater concentrations as shown in the depth bins of Table 2 to approximately 600 m. The *Far-field* is depicted as the array of particles extending from the *Near-field*. *C18A* is approximately 31 km × 7 km × 200 m.

For example, the more positive (heavier) values of $\delta^{18}O$ are found closer to the coasts in Antarctic ice-sheets and ice-shelves at the surface [*Morgan*, 1982]. Presumably, this reflects the earlier rain-out of heavier water before the drier, lighter air reaches the interior of the content. Further, ice-shelf thinning by basal melting may remove the more continental ice (more depleted) from the bottom of the ice-shelf before calving occurs [*Rignot*, 2008]. Thus the relatively enriched ice formed from near-coastal precipitation would be what is released as icebergs. Additionally, *C18A* likely spent at least some decades at the coast before calving and, from satellite observations, we know that *C18A* spent at least 7 years drifting in the circumpolar countercurrent before we sampled it.

4.3. Implications of Meltwater Field Production

It appears that there are three distinct geophysical processes at work as a result of iceberg transit in this setting: (1) subaerial ablation, (2) sidewall and basal melting, and (3) deep, turbulent mixing, and advection (Figure 3). We hypothesize that there are two densification mechanisms, one dominated by surface cooling and another dominated by mixing the cooled water with high-salinity WDW, induced by mechanical turbulence. This would create upwelling due to mass conservation [*Neshyba*, 1977] resulting in convection carrying AASW and WW down and WDW upward. The deep penetration of the meteoric water signal to 600 m is an effect of these mixing processes. This is consistent with the XBT and ADCP observations that the pycnocline was disrupted to 1500 m [*Helly et al*., 2011a]. We theorize that the mechanism for this is the differential distribution of heat and salt combined with the mechanical disturbance of the iceberg moving through the pycnocline by freshening, cooling, and turbulence resulting in mixing to a surprising depth.

A related implication of the geophysical processes is that iceberg ablation releases and distributes iceberg-derived inorganic terrestrial debris [*Smith*, 2011b] that is mixed as a consequence of the hypothesized densification mechanisms. This results in modified surface water that is relatively rich in inorganic nutrients and has a higher transmissivity in the euphotic zone [*Vernet et al*., 2011]. Importantly, these conditions can set up a transient environment for enhanced phytoplankton growth [*Schwarz and Schodlok*, 2009; *Vernet et al*., 2011], until the disturbed waters reequilibrate to ambient conditions.

4.4. Comparison to Other Iceberg Ablation Rate Estimates

Based on satellite observations, *Scambos et al*. [2008] found that large, tabular icebergs in the open ocean experience a steady loss of area ranging from (1–2) to (3–10) $\times 10^4$ $m^2 km^{-1} d^{-1}$. Applying this to *C18A* calculation results in an ablation rate of 1.2%day^{-1} at the high-end; assuming that this mass loss is converted to meltwater as opposed to additional icebergs. While this is the same order of magnitude as our estimate, 0.4% day^{-1}, it may reflect a focus on actively calving icebergs rather than a more continuous ablation dominated by melting. Additionally, variations in ablation rates can occur as a function of how much of its lifetime an iceberg spends in sea ice; constraining the AASW to the freezing point and slowing the ablation rate.

5. Conclusion

Our results support the hypothesis that the ablation of icebergs establishes a transiently stable lens of an ambient seawater and fresh meltwater mixture astern of an iceberg, in the euphotic zone, that gradually mixes away in the wake over a period of days to weeks at a spatial scale of tens of kilometers. These effects suggest an important role for icebergs in determining the structure of the water column and provides a picture of the spatial and temporal scales of the dynamic processes around icebergs and their potential interactions with the local biogeochemistry. This is a new view of the dynamics of the iceberg ecosystem described in *Vernet et al*. [2012]. Our conceptual model provides the basis for future estimates of (i) the coupling between iceberg geophysics and the biogeochemistry of carbon-cycling related to iron-production and phytoplankton growth and (ii) the scaling of the geophysical and biogeochemical effects to regional and global domains.

Acknowledgments
We thank the Captain and crew, the Raytheon logistics, and technical support team on the RVIB Nathaniel B. Palmer (NBP0902) for excellent precruise and field support and our colleagues in the science party for their interdisciplinary collaboration. We also thank the Editor and three anonymous peer-reviewers whose critical and constructive comments resulted in substantial improvements to the manuscript. This research was supported by NSF grants ANT-0636723, ANT-0636730, and ANT-0636543. Data may be obtained by corresponding with J. Helly.

References

Ballantyne, J. (2002), *A multidecadal study of the number of Antarctic icebergs using scatterometer data*, BYU online report. [Available at http://www.scp.byu.edu/data/iceberg/IcebergReport.pdf.]
Cavalieri, D. J., and C. L. Parkinson (2008), Antarctic sea ice variability and trends, 1979–2006, *J. Geophys. Res.*, *113*, C07004, doi:10.1029/2007JC004564.
Cleveland, W. S. (1979), Robust locally weighted regression and smoothing scatterplots, *J. Am. Stat. Assoc.*, *74*(368), 829–836, doi:10.2307/2286407.
Coplen, T. B. (1994), Reporting of stable hydrogen, carbon, and oxygen isotopic abundances, *Pure Appl. Chem.*, *66*, 273–276.
Epstein, S., and T. Mayeda (1953), Variation of ^{18}O content of water from natural sources, *Geochim. Cosmochim. Acta*, *4*, 213–224.
Garabato, A. C. N., E. L. McDonagh, D. P. Stevens, K. J. Heywood, and R. J. Sanders (2002), On the export of Antarctic Bottom Water from the Weddell Sea, *Deep Sea Res., Part II*, *49*(21), 4715–4742, doi:10.1016/S0967-0645(02)00156-X.
Gladstone, R. M., G. R. Bigg, and K. W. Nicholls (2001), Iceberg trajectory modeling and meltwater injection in the southern ocean, *J. Geophys. Res.*, *106*(C9), 19,903–19,915.
Grootes, P. M., and M. Stuiver (1983), Ross Ice Shelf oxygen isotope profile at j-9, *Antarct. J.*, *XVIII*(5), 107–108.
Helly, J. J., R. S. Kaufmann, G. R. Stephenson Jr., and M. Vernet (2011a), Cooling, dilution and mixing of ocean water by free-drifting icebergs in the Weddell Sea, *Deep Sea Res., Part II*, *58*(11–12), 1346–1363, doi:10.1016/j.dsr2.2010.11.010.
Helly, J. J., R. S. Kaufmann, M. Vernet, and G. R. Stephenson (2011b), Spatial characterization of the meltwater field from icebergs in the Weddell Sea, *Proc. Natl. Acad. Sci. U. S. A.*, *108*(14), 5492–5497.
Jacobs, S. S., and R. G. Fairbanks (1984), Origin and evolution of water masses near the Antarctic continental margin: Evidence from $H_2{}^{18}O/H_2{}^{16}O$ ratios in seawater, *Oceanol. Antarct. Cont. Shelf*, *43*, 59–85.
Jenkins, A. (1999), The impact of melting ice on ocean waters, *J. Phys. Oceanogr.*, *29*, 2370–2381.
Jenkins, A., and S. Jacobs (2008), Circulation and melting beneath George VI Ice Shelf, Antarctica, *J. Geophys. Res.*, *113*, C04013, doi:10.1029/2007JC004449.
Kristensen, M. (1983), Iceberg calving and deterioration in Antarctica, *Prog. Phys. Geogr.*, *7*, 313–328.
Lazzara, M. A., K. C. Jezek, T. A. Scambos, D. R. MacAyeal, and C. J. van der Veen (1999), On the recent calving of icebergs from the ross ice shelf 1, *Polar Geogr.*, *23*(3), 201–212, doi:10.1080/10889379909377676.
Lehmann, M., and U. Siegenthaler (1991), Equilibrium oxygen- and hydrogen-isotope fractionation between ice and water, *J. Glaciol.*, *37*(125), 23–26.
Lin, H., S. Rauschenberg, C. R. Hexel, T. J. Shaw, and B. S. Twining (2011), Free-drifting icebergs as sources of iron to the Weddell Sea, *Deep Sea Res., Part II*, *58*(11–12), 1392–1406.
Long, D. G., J. Ballantyne, and C. Bertoia (2002), Is the number of icebergs really increasing?, *EOS Trans. AGU*, *83*(42), 469–474, doi:10.1029/2002EO000330.
McDougall, T. J. (1990), Bulk properties of "hot smoker" plumes, *Earth Planet. Sci. Lett.*, *99*(1–2), 185–194.
Meredith, M. P., M. A. Brandon, M. I. Wallace, A. Clarke, M. J. Leng, I. A. Renfrew, N. P. van Lipzig, and J. C. King (2008), Variability in the freshwater balance of northern Marguerite Bay, Antarctic Peninsula: Results from $\delta^{18}O$, *Deep Sea Res., Part II*, *55*, 309–322, doi:10.1016/j.dsr2.2007.11.005.
Morgan, V. (1982), Antarctic ice sheet surface oxygen isotope values, *J. Glaciol.*, *28*(99), 315–323.
Neshyba, S. (1977), Upwelling by icebergs, *Nature*, *267*, 507–508.
NIST (2012), *Engineering Statistics Handbook*,
Oerter, H., J. Kipfstuhl, J. Determann, H. Miller, D. Wagenbach, A. Minikin, and W. Graft (1992), Evidence for basal marine ice in the Filchner-Ronne ice shelf, *Nature*, *358*(6385), 399–401.
Orheim, O. (1988), Antarctic icebergs—Production, distribution and disintegration [abstract], *Ann. Glaciol.*, *11*, 205.
Pisarevskaya, L., and V. A. Volkov (2007), Tornado-like structures under the iceberg in the Barents Sea, *Probl. Ark. Antarkt.*, *77*, 56–66.
Pisarevskaya, L. G., and I. K. Popov (1991), Free-drifting icebergs and thermohaline circulation, in Glaciers-Ocean-Atmosphere Interactions, Proceedings of International Symposium, St Petersburg, September 1990, IAHS Publ., vol. 208, pp. 447–454.
R Development Core Team (2008), *R: A Language and Environment for Statistical Computing*, R Found. for Stat. Comput., Vienna.
Révész, K., and T. B. Coplen (2008), Determination of the $\delta(^{18}O/^{16}O)$ of water, Methods of the Reston Stable Isotope Laboratory, *Tech. Rep. 28*, U.S. Geol. Surv. Tech. and Methods.
Rignot, E., S. Jacobs, J. Mouginot, and B. Scheuchl (2013), Ice-shelf melting around Antarctica, *Science*, *341*(6143), 266–270.
Rignot, E. B. (2008), Antarctic ice mass loss from radar interferometry and regional climate modelling, *Nat. Geosci.*, *1*, 106–110.
Scambos, T., O. Sergienko, A. Sargent, D. MacAyeal, and J. Fastook (2005), Icesat profiles of tabular iceberg margins and iceberg breakup at low latitudes, *Geophys. Res. Lett.*, *32*, L23S09, doi:10.1029/2005GL023802.
Scambos, T., R. Ross, R. Bauer, Y. Yermolin, P. Skvarca, D. Long, J. Bohlander, and T. Haran (2008), Calving and ice-shelf break-up processes investigated by proxy: Antarctic tabular iceberg evolution during northward drift, *J. Glaciol.*, *54*(187), 579–591.

Schodlok, M. P., H. H. Hellmer, O. Rohardt, and E. Fahrbach (2006), Weddell Sea iceberg drift: Five years of observations, *J. Geophys. Res.*, *111*, C06018, doi:10.1029/2004JC002661.
Schwarz, J. N., and M. P. Schodlok (2009), Impact of drifting icebergs on surface phytoplankton biomass in the southern ocean: Ocean colour remote sensing and in situ iceberg tracking, *Deep Sea Res.*, Part I, *56*, 1727–1741.
Silva, T., G. Bigg, and K. Nicholls (2006), The contribution of giant icebergs to the Southern Ocean freshwater flux, *J. Geophys. Res.*, *111*, C03004, doi:10.1029/2004JC002843.
Smith, J. K. L. (Ed.) (2011a), Free-drifting icebergs in the Southern Ocean, *Deep Sea Res., Part II*, *58*, 1277–1504.
Smith, K. L., Jr. (2011b), Free-drifting icebergs in the Southern Ocean: An overview, *Deep Sea Res.*, Part II, *58*(11–12), 1277–1284.
Stephenson, G. R., Jr., J. Sprintall, S. T. Gille, M. Vernet, J. J. Helly, and R. S. Kaufmann (2011), Subsurface melting of a free-floating Antarctic iceberg, *Deep Sea Res., Part II*, *58*(11–12), 1336–1345.
Stuart, K., and D. Long (2011), Tracking large tabular icebergs using the SeaWinds Ku-band microwave scatterometer, *Deep Sea Res., Part II*, *58*(11–12), 1285–1300, doi:10.1016/j.dsr2.2010.11.004.
Thompson, A. F., K. J. Heywood, S. E. Thorpe, A. H. H. Renner, and A. Trasviña (2009), Surface circulation at the tip of the Antarctic Peninsula from drifters, *J. Phys. Oceanogr.*, *39*(1), 3–26, doi:10.1175/2008JPO3995.1.
Timco, G. W., and R. Frederking (1996), A review of sea ice density, *Cold Reg. Sci. Technol.*, *24*, 1–6.
Tournadre, J., F. Girard-Ardhuin, and B. Legresy (2012), Antarctic icebergs distributions, 2002–2010, *J. Geophys. Res.*, *117*, C05004, doi:10.1029/2011JC007441.
Vernet, M., K. Sines, D. Chakos, A. O. Cefarelli, and L. Ekern (2011), Impacts on phytoplankton dynamics by free-drifting icebergs in the NW Weddell Sea, *Deep Sea Res., Part II*, *58*(11–12), 1422–1435.
Vernet, M., et al. (2012), Islands of ice: Influence of free-drifting Antarctic Icebergs on pelagic marine ecosystems, *Oceanography*, *25*(3), 38–39.
Wadhams, P. (2000), *Ice in the Ocean*, pp. xi + 351, Gordon and Breach.
Weiss, R. F. (1979), Geochemical studies of the Weddell Sea, *Deep Sea Res., Part A*, *26*, 1093–1120.
Williams, R. N., W. G. Rees, and N. W. Young (1999), A technique for the identification and analysis of icebergs in synthetic aperture radar images of Antarctica, *Int. J. Remote Sens.*, *20*(15–16), 3183–3199.
Worby, A. P., C. A. Geiger, M. J. Paget, M. L. V. Woert, S. F. Ackley, and T. L. DeLiberty (2008), Thickness distribution of Antarctic sea ice, *J. Geophys. Res.*, *113*, C05S92, doi:10.1029/2007JC004254.